



Machine and Deep Learning in Hyperspectral Fluorescence-Guided Brain Tumor Surgery

Eric Suero Molina, David Black, Andrew Xie, Jaidev Gill, Antonio Di Ieva, and Walter Stummer

Abstract

Malignant glioma resection is often the first line of treatment in neuro-oncology. During glioma surgery, the discrimination of tumor's

- E. Suero Molina (✉)
Computational NeuroSurgery (CNS) Lab, Macquarie Medical School, Faculty of Medicine, Human and Health Sciences, Macquarie University, Sydney, NSW, Australia
Macquarie Neurosurgery & Spine, MQ Health, Macquarie University Hospital, Sydney, NSW, Australia
Department of Neurosurgery, University Hospital Münster, Münster, Germany
e-mail: e.suero@uni-muenster.de
- D. Black · A. Xie · J. Gill
Department of Electrical and Computer Engineering, University of British Columbia, Vancouver, BC, Canada
- A. Di Ieva
Computational NeuroSurgery (CNS) Lab, Macquarie Medical School, Faculty of Medicine, Human and Health Sciences, Macquarie University, Sydney, NSW, Australia
Macquarie Neurosurgery & Spine, MQ Health, Macquarie University Hospital, Sydney, NSW, Australia
Department of Neurosurgery, Nepean Blue Mountains Local Health District, Kingswood, NSW, Australia
Centre for Applied Artificial Intelligence, School of Computing, Macquarie University, Sydney, NSW, Australia
- W. Stummer
Department of Neurosurgery, University Hospital Münster, Münster, Germany

edges can be challenging at the infiltration zone, even by using surgical adjuncts such as fluorescence guidance (e.g., with 5-aminolevulinic acid). Challenging cases in which there is no visible fluorescence include lower-grade gliomas, tumor cells infiltrating beyond the margin as visualized on pre- and/or intraoperative MRI, and even some high-grade tumors. One field of research aiming to address this problem involves inspecting in detail the light emission spectra from different tissues (e.g., tumor vs. normal brain vs. brain parenchyma infiltrated by tumor cells). Hyperspectral imaging measures the emission spectrum at every image pixel level, thus combining spatial and spectral information. Assuming that different tissue types have different "spectral footprints," eventually related to higher or lower abundances of fluorescent dyes or auto-fluorescing molecules, the tissue can then be segmented according to type, providing surgeons a detailed spatial map of what they see. However, processing from raw hyperspectral data cubes to maps or overlays of tissue labels and potentially further molecular information is complex. This chapter will explore some of the classical methods for the various steps of this process and examine how they can be improved with machine

learning approaches. While preliminary work on machine learning in hyperspectral imaging has had relatively limited success in brain tumor surgery, more recent research combines this with fluorescence to obtain promising results. In particular, this chapter describes a pipeline that isolates biopsies in ex vivo hyperspectral fluorescence images for efficient labeling, extracts all the relevant emission spectra, preprocesses them to correct for various optical properties, and determines the abundance of fluorophores in each pixel, which correspond directly with the presence of cancerous tissue. Each step contains a combination of classical and deep learning-based methods. Furthermore, the fluorophore abundances are then used in four machine learning models to classify tumor type, WHO grade, margin tissue type, and isocitrate dehydrogenase (IDH) mutation status in brain tumors. The classifiers achieved average test accuracies of 87%, 96.1%, 86%, and 93%, respectively, thus greatly outperforming prior work both with and without fluorescence. This field is new, but these early results show great promise for the feasibility of data-driven hyperspectral imaging for intraoperative classification of brain tumors during fluorescence-guided surgery.

Keywords

Artificial intelligence · Machine learning · Hyperspectral imaging · Fluorescence-guided surgery

1 Introduction

Maximal resection of brain tumors significantly impacts the survival of patients harboring malignant gliomas [1] but remains challenging. To improve resection rates, 5-aminolevulinic acid (5-ALA)-mediated fluorescence guidance is a surgical adjunct in the resection of brain tumors that uses fluorescent protoporphyrin IX (PpIX)

to visualize and resect gliomas. Patients orally ingest 20 mg/kg b.w. of 5-ALA preoperatively, which is preferentially metabolized by malignant gliomas into the fluorescent biomarker PpIX (Fig. 1). PpIX is excited by blue light at around 405 nm and fluoresces bright red with a main peak at 634 nm [1, 2]. During surgery, PpIX fluorescence can guide tumor resection, leading to maximized resection and improved progression-free and overall survival [3, 4]. However, the visibility of PpIX fluorescence is poor in low-grade gliomas (LGGs) and tumor margins. Moreover, increasing the sensitivity of the imaging system does not lead to better visualization of PpIX because other endogenous fluorophores, which contribute to autofluorescence and are not indicative of malignant cells, exhibit fluorescence at magnitudes and spectral ranges similar to the weakly fluorescing PpIX. To address these challenges, hyperspectral imaging (HSI) has been utilized to capture more information and enhance PpIX detection in fluorescence-guided resection (FGR) of brain tumors.

Hyperspectral imaging captures not only red, green, and blue bands as is accustomed in RGB cameras, but rather it collects the entire light emission spectrum over a particular spectral range at every pixel. The following section describes this in detail and gives information about the tissue than visual inspection. For example, with a priori knowledge of the emission spectra of individual compounds, the hyperspectral images can be used to determine which compounds are present and their corresponding fractional abundances through spectral unmixing (Sect. 7). This process allows trace amounts of PpIX to be isolated among other fluorophores, or the distribution of fluorophores can be used to classify and describe the tissue. Alternatively, the raw spectra themselves can be used to perform such computations. In this way, HSI produces very rich information about the tissue.

HSI has thus been used extensively in satellite imaging [5], agriculture [6], forestry [7], and food science [8]. More recently, myriads of medical applications have been explored, including dermatology [9] and breast cancer [10]. Surgical

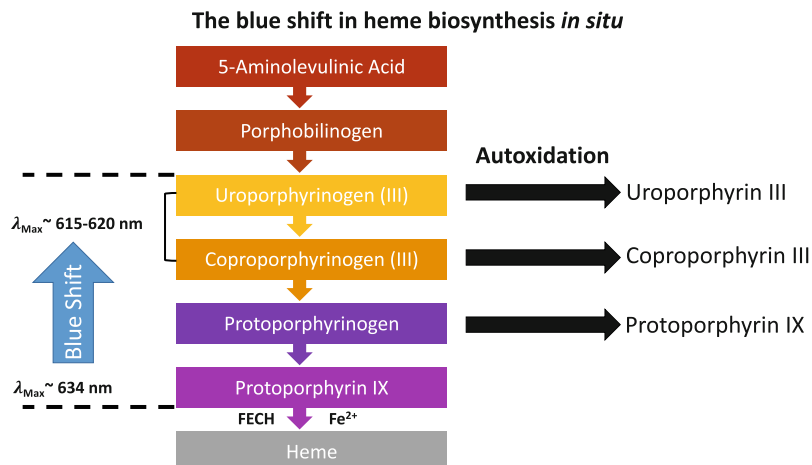


Fig. 1 Heme biosynthesis and fluorescence peak maxima. (Reprinted with permission CC BY 4.0 [2])

hyperspectral imaging is reviewed by Clancy et al. [11]. In most applications, HSI is used to perform semantic segmentation using the spectra [12–15] or to determine specific properties of the objects, for example, blood oxygenation of tissue during surgery [16]. This is effective because HSI creates very rich data; however, as a result, the output of an HSI image acquisition is a very large, high-dimensional dataset. For example, in a system with 100 spectral bands, capturing a 512×512 pixel image with 32-bit depth at every band, a single acquisition consists of 26,214,400 numbers or 105 MB of data. Classical methods exist to process this data and obtain dimensionally reduced representations, such as fluorophore abundances at every pixel. Some of these are described in the following sections. However, these techniques are imperfect, and their output is still an n-dimensional image, where n is the number of fluorophores considered. For classification, segmentation, or regression tasks on such data, deep learning is likely the most effective approach [17].

Deep learning in hyperspectral imaging without fluorescence has been reviewed by Jia et al. [18] and for medical applications specifically by Cui et al. [19] and Khan et al. [20]. In brain tumor surgery, the technique is promising and is even being pursued by a startup company, HyperVision Surgical (London, UK) [21]. Multiple studies attempting to use HSI to segment and classify the

different tissues present in vivo exist. Urbanos et al. tested several machine learning methods, including support vector machines (SVMs) and random forest models, and simple convolutional neural networks (CNNs) to perform segmentation on datasets of 13 [22, 23] and 26 images [24]. Other researchers have used majority voting-based fusions of k-nearest neighbors (KNN), hierarchical k-means clustering, and dimensionality reduction techniques such as principal component analysis (PCA) or t-distributed stochastic neighbor embedding (t-SNE) with good results [25, 26]. These papers used 61 images from 34 patients and achieved a median macro F1-score of 70%. A mixture of KNN and a multilayer perceptron (MLP) was also employed by Rinesh et al. [27]. Several groups have used the HELICoID (Hyperspectral Imaging Cancer Detection) dataset [28], which contains 36 hyperspectral images from 22 different patients. For example, Manni et al. used a CNN architecture to achieve 80% accuracy in classifying tumor, healthy tissue, and blood vessel [29], and Hao et al. fused several deep learning architectures in a multistep process to achieve 96% accuracy in glioblastoma identification [30]. This greatly outperforms other methods used on pathological slides [31] and very small datasets [32]. Finally, Kifle et al. found higher accuracy when using a random forest classifier on RGB images rather than HSI data, which suggests a problematic dataset as HSI data contains strictly

more information than RGB data and thus should at least match its performance [33].

Thus, though many interesting papers have been published, almost none have yet achieved clinically relevant performance, with typical accuracies between 60% and 80%. This is likely in part due to small datasets, costly labeling of HSI images, and consequent limited use of modern deep learning architectures for medical image segmentation, such as U-Net [34], V-Net [35], and graph neural networks (GNNs) [36]. Generative adversarial networks (GANs) [37] and encoder-decoder models [38] can use weakly supervised or unsupervised learning to avoid the labeling problem but necessitate big datasets. A further reason for the unsatisfactory performance is that none of the aforementioned papers used fluorescence in combination with HSI. Indeed, most of them were trained and tested only on glioblastoma, which are high grade and usually fluoresce visibly anyway when using fluorescence guidance [1, 3, 39]. The real challenges are detecting and classifying infiltrating margins, low-grade glioma, and/or other tumor types and determining clinically essential markers such as the IDH mutation status (i.e., mutant vs. wildtype).

To this end, recent papers by Leclerc et al. [40] and Black et al. [41, 42] have combined fluorescence, HSI, and machine learning with promising results. This chapter, therefore, summarizes the authors' experience in analyzing hyperspectral fluorescence images using a relatively larger dataset from brain tumor resections (Table 1) to perform these tasks. Our objective is to address the limitations of prior techniques by adopting a data-driven approach that incorporates machine and deep learning algorithms where appropriate, ultimately resulting in improved accuracy, clarity, and clinical utility of resulting overlays. Therefore, the following sections first outline hyperspectral fluorescence imaging (Sect. 2) and the processing pipeline (Sect. 3), highlighting which steps of the process can be improved using data-driven methods. Each of these steps is then discussed in detail in the following sections, exploring both the classical and machine learning methodologies.

2 Hyperspectral Fluorescence Imaging

In regular cameras, each pixel is sensitive to either red, green, or blue light. RGB images are produced through interpolation and demosaicking. In HSI, on the other hand, many narrow spectral bands are captured across the visible spectrum or beyond it into near-infrared (NIR) and/or ultra-violet (UV). The different technologies used to acquire these images are described briefly in Sect. 4. Each ultimately produces a stack of grayscale images, each capturing the light from one section of the spectrum. This stack, known as a data cube, thus contains all the present spatial and spectral information. An example is shown in Fig. 2. In fluorescence imaging, each pixel contains the emission spectrum from that point. As shown in Fig. 2, the spectrum looks very different depending on what is present in the pixel; a strongly fluorescing region shows a clean PpIX spectrum, while a weakly fluorescing area has similar proportions of PpIX and autofluorescence. Our system, described in Sect. 4, captures ex vivo tissue biopsies and averages the spectra of 10×10 pixel regions to decrease noise. Thus, depending on size, each biopsy can yield up to several thousand spectra.

Each spectrum consists of a combination of all the present fluorescing compounds or fluorophores. A priori knowledge of the fluorophores' emission spectra enables the decomposition of the measured spectra into the constituent spectral signatures (endmembers) stemming from different fluorophores [43]. This is known as spectral unmixing and is described in Sect. 7. The endmembers include PpIX and endogenous fluorophores such as lipofuscin, NADH, collagen, and flavins, collectively termed autofluorescence. By studying the distribution of fluorophores in a given pixel, this method can provide much more information than visual inspection. Additionally, by giving 5-ALA prior to surgery, the enhanced presence of PpIX in tumor cells further facilitates tumor tissue classification.

Table 1 Breakdown of data from the analysis presented in this chapter

Classification type	# of data cubes	Classification type	# of data cubes
<i>Tumor type</i>	632	<i>Margin type (gliomas)</i>	288
Pilocytic astrocytoma	5	Reactively altered brain tissue	100
Diffuse astrocytoma	57	Infiltrating zone	57
Anaplastic astrocytoma	51	Solid tumor	131
Glioblastoma	410		
Grade II oligodendrogloma	24	<i>WHO grade (gliomas)</i>	571
Ganglioglioma	4	Grade I	9
Medulloblastoma	6	Grade II	84
Anaplastic ependymoma	8	Grade III	57
Anaplastic oligodendrogloma	4	Grade IV	421
Meningioma	37		
Metastasis	6	<i>IDH classification</i>	411
Radiation necrosis	20	IDH mutant	126
		IDH wildtype	285

This comes from 891 hyperspectral data cubes of ex vivo tissue from fluorescence-guided surgeries of 184 patients. Not every data cube had information on all the classifications, hence the varying number of data cubes in each. In the margin classification, reactively altered brain tissue (RABT) is tissue outside of the infiltration zone and can be considered the “normal tissue”

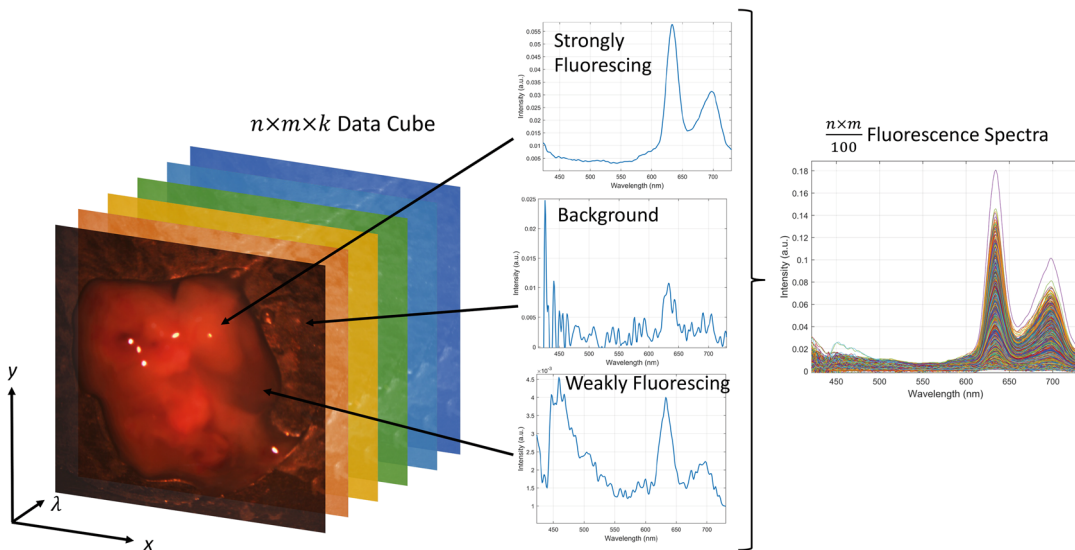


Fig. 2 Hyperspectral imaging illustration. In HSI, a stack of images is captured, each from successive narrow spectral bands. In our case, these range from 421 to 730 nm in 3 nm steps. Each pixel of the resulting data cube contains

the entire light spectrum, and these are averaged over 10×10 regions of pixels to reduce noise. The spectra differ greatly depending on the material present in the region

3 Overall Pipeline and Data-Driven Opportunities

Due to the complex, high-dimensional nature of the output data, the processing pipeline after im-

age acquisition is relatively complex. Extensive literature on this topic exists [44, 45], and this chapter will only cover the essentials of HSI processing for fluorescence-guided brain tumor resection specifically. The overall pipeline is shown in Fig. 4. Each step that can be augmented by

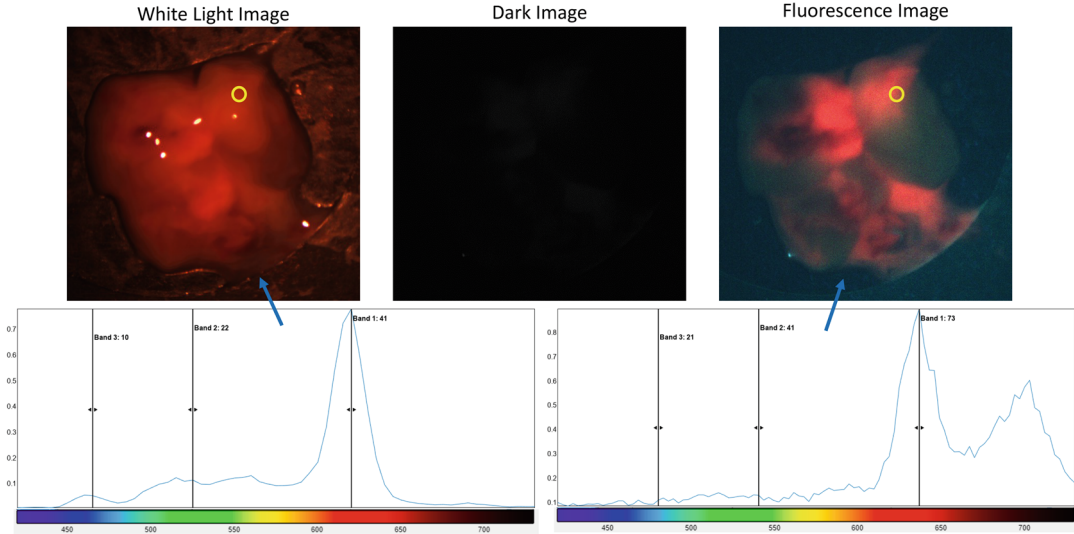


Fig. 3 Outputs from one hyperspectral measurement of a brain tumor biopsy. The images are false-color RGB representations of the data cubes with the red, green, and

blue taken at the three bands shown in the spectra. The strong red in the right-hand image shows fluorescence of malignant tumor

data-driven approaches is bolded and described in the following sections.

The output of a hyperspectral fluorescence measurement usually consists of a data cube measured under white-light illumination, a fluorescence data cube measured under blue light illumination, and a dark data cube measured with no illumination. These are shown in Fig. 3, and the image acquisition process is examined in Sect. 4. The dark cube is subtracted from the other two to reduce the dark noise from the camera sensor. After this, the fluorescence spectra are normalized using the white-light spectra. This accounts for the heterogeneous optical and geometric properties of the imaged tissue and is described in Sect. 6. Several other preprocessing steps are device-specific, including correcting for the wavelength-dependent camera sensitivity, vignetting, and varying pass bands of the tunable band-pass filter, if one is used. These are not described in detail.

The normalized and corrected fluorescence data cubes can either be used directly to perform deep convolutional network-based segmentation, classification, and/or regression, or they can be

spectrally unmixed to determine the fluorophore abundances. This is described in Sect. 7. After unmixing, classifiers are applied to the abundance vectors, as described in Sect. 8. The ultimate output is an overlay heatmap of tissue type, malignancy, or other markers being classified.

In order to improve these steps using machine learning, large datasets are, of course, required. Our HSI system has been described previously [39, 46–48].

During fluorescence-guided surgeries, resected pieces of brain tumor or other tissue were immediately imaged ex vivo with the HSI device before being sent for histopathological assessment. In this way, we have collected 891 hyperspectral fluorescence data cubes from 184 patients, totaling approximately 555,666 high-quality fluorescence spectra. These stem from patients with a wide variety of different pathologies, outlined in Table 1. To extract and label the spectra, a computer vision system was developed to segment the tumors in the images. This is described in Sect. 5. The purple dashed lines in Fig. 4 show all the steps where this data can be used.

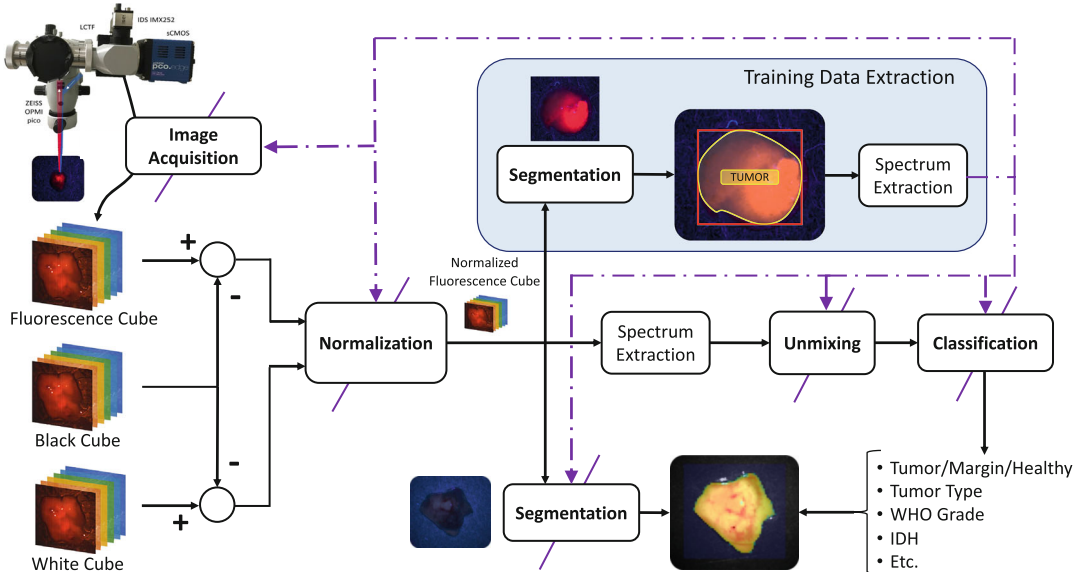


Fig. 4 The entire processing pipeline, from image acquisition to high-level image segmentation, classification, and even analysis of biomarkers such as IDH mutation. The

bolded steps of the process are described in detail in the following sections. Each step can be tuned and improved using data-driven methods with data extracted from many measurements, as shown in the blue box

4 Image Acquisition

Three main types of HSI devices exist, differing in how they acquire the images [49]. In spatial scanning devices, light passes through a narrow slit and is dispersed with a grating or lens onto a sensor. Thus, one line of the data cube is captured at a time, and a push-broom scanner moves the slit to capture the whole image [50]. A similar system captures one point at a time through an optical fiber and scans in two axes to create the image. Conversely, in spectral scanning devices, a grayscale camera captures the whole scene, but the light is first filtered through a tunable optical band-pass filter. As the pass band is swept across the spectral range, a series of images is captured. Such a system is shown in Fig. 5. It consists of a light source for blue and white illumination, an objective lens for capturing the wide-field light, a high-pass filter to remove the brightly reflected blue excitation light, a liquid crystal tunable filter (LCTF), and a scientific metal oxide semiconductor (sCMOS) camera. This captures 104 spectral bands with a step size of 3 nm and very high

spatial resolution. However, the acquisition time is more than two minutes, so it is not suitable for intraoperative use.

While spatial scanning systems have good spectral resolution, the spatial resolution is proportional to acquisition time. The spatial resolution for spectral scanning devices can be very high, but it takes time for each tuning of the pass band. Additionally, the band-pass filter has an approximately Gaussian transmission curve centered at the desired wavelength and with a given finite bandwidth. Thus, light attributed to a certain wavelength is actually a weighted integral of light coming from a range around that wavelength. This slightly degrades the accuracy of the measured spectra.

Given the time-consuming acquisition, the third HSI device type is called a snapshot HSI camera. This captures the spatial and spectral information in a single shot and can be used in real-time scenarios. Various interesting devices exist to achieve this [51–53]. However, most commercially available snapshot cameras have repeated arrays of around 9–16 pixels, each sensitive to a different spectral band, much like

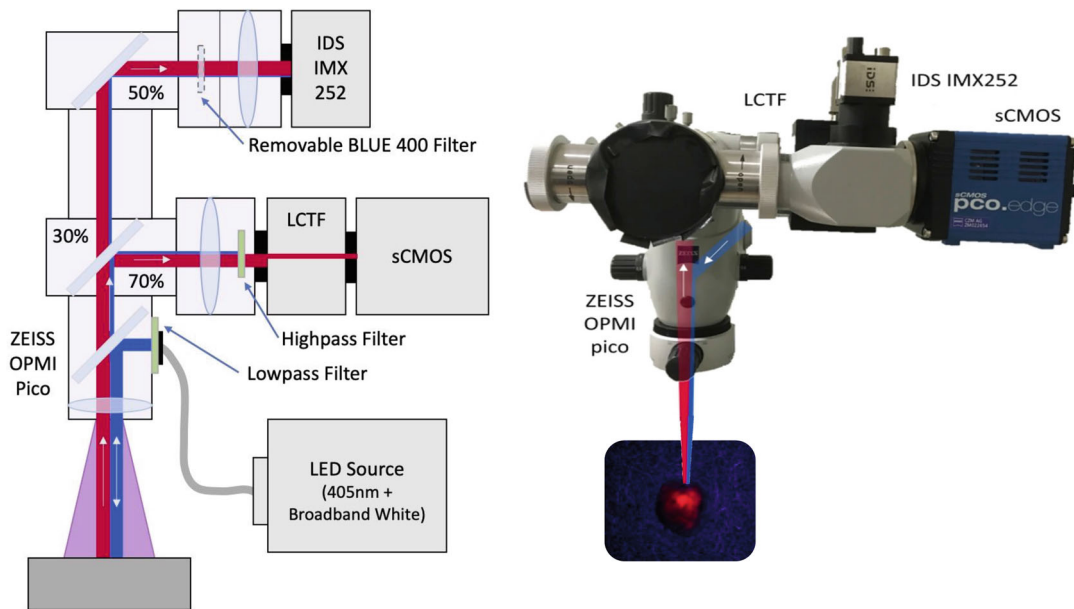


Fig. 5 The hyperspectral measurement device consists of a microscope objective, an LCTF, and an sCMOS camera. A low-pass optical filter is used to excite the tissue with

only 405 nm blue light, and a high-pass filter is used to remove the intense reflected excitation light from the image while allowing the weak, red fluorescence

RGB cameras. Thus, the spatial resolution is down-sampled by a factor of 3–4 in both axes, and the spectral resolution is only 9–16 bands over the whole spectrum. This leads to relatively low spatial and spectral resolution.

To overcome these limitations in HSI image acquisition, it is necessary either to reduce the number of bands required for a spectral scanning image or to demosaic the heavily down-sampled snapshot images more effectively. Machine learning can help in both cases. For the former approach, it is observed that certain spectral regions contain most of the information about the PpIX fluorescence. Thus, capturing only these bands should not greatly reduce the relevant information content of the data cubes. To this end, Martinez et al. used a genetic algorithm to determine an optimal value of 48 bands, achieving 5% better classification accuracy than with 128 bands [54]. Subsequently, Baig et al. introduced a method using empirical mode decomposition to determine the most relevant bands [55], leading to a sevenfold decrease in the data dimensionality. This reduced dataset (7 bands) performed equally well as the benchmark dataset (48 bands) on a tumor

classification task using SVM. Even with only the three optimal bands, the performance decreased by only 10%. Giannantonio et al. used neural networks to optimize the number of bands and precision simultaneously [56]. From 104 bands, they compressed the acquisition to 3, 6, or 12 bands based on data from 5 patients. With 12 bands, the performance of an MLP classifier is comparable to the original, while with 3 bands, accuracy again drops by about 10%. Further work in this direction may enable good performance and real-time intraoperative use while maintaining high spatial resolution.

The other approach is to demosaic the snapshot images using deep learning-based hyper-resolution techniques. Li et al. have explored this, first using CNNs [57] and subsequently with a novel unsupervised learning approach that employs inter-spectral band regularization based on spatial gradient consistency [58]. This achieves results similar to supervised learning without requiring large ground truth datasets and greatly outperforms linear interpolation. Such techniques may enable clinical use of high-speed snapshot devices. Other practical improvements are also

possible using machine learning, for example, performing auto-focusing in HSI devices using deep reinforcement learning [59]. This method reduced mean focal error by a factor of two. Thus, data-driven approaches can be valuable for hyperspectral image acquisition.

5 Data Preparation

Once the data cubes are acquired, the next step in our pipeline is to segment the ex vivo tumor images automatically. This enables analysis of the spectra, as well as integration of the new data into our dataset without inadvertently including spectra of the slide background. The challenge is that smears of fluid, irregular and sometimes disjoint shapes, and very bright reflections confound the otherwise simple segmentation task. It would be possible to use the total fluorescence spectra to perform the classification. However, for speed and simplicity, we used a single band around 634 nm, the primary fluorescence peak of PpIX, and a Detectron2-based classifier [60]. The architecture was pre-trained, for instance, segmentation on very broad input data, and we subsequently trained it on our data to recognize the tumor biopsies. With this simple approach, intersection over union (IoU) tests give an average precision at $\text{IoU} = 0.5$ of 98.82% and at $\text{IoU} = 0.75$ of 96.54%. With quick manual checks of the images before integration into our dataset, this was sufficiently accurate (Fig. 6). However, using more of the available spectrum can, of course, greatly improve the performance. While this is only for extracting and curating our dataset, tumor segmentation in in vivo fluorescence images is crucial for future work.

6 Normalization and Preprocessing

Having obtained and extracted the emission spectra, the data must be preprocessed and normalized. As mentioned in Sect. 3, the several steps of device-specific preprocessing include correcting

for the wavelength-dependent camera sensitivity, for vignetting, and for the varying pass bands of the tunable band-pass filter. These are not described here as they vary with the HSI system.

More relevant is the normalization of the fluorescence spectra. As shown in Fig. 7, tumor biopsies and in vivo tissues have very heterogeneous optical properties across the surface. Some regions are shaded, while others have bright specular reflectance. This leads to relatively large variations in the measured intensity of the spectra from the different regions, even if the fluorophore abundances are actually uniform across the measurement. Correcting for this phenomenon is referred to here as normalization. In vivo, the three-dimensional geometry also leads to variations since pixels further from the objective lens will appear less bright than the closer ones. This also has to be corrected for, but in our data the biopsies are small and relatively flat, so this is less relevant.

The current method for normalization involves extracting a correction factor from the white-light spectrum and using it to scale the fluorescence spectrum [61]. The factor is found by integrating over two sections of the white spectrum, one representing the excitation wavelength band of PpIX and the other the emission band. One band is exponentiated with an empirically derived exponent, and the two are then multiplied together. This was effective in phantom tests with varying optical scattering and absorption coefficients in these bands [62]. The R^2 values for the linearity of intensity versus PpIX concentration increased from 0.27 to 0.88 using dual-band normalization. However, the technique's effectiveness in human tissue is relatively unproven. Furthermore, optimizing the two band locations leads to bands well outside the emission or excitation ranges of PpIX, which seemingly contradicts the theoretical basis of the method. It is also likely that this linear scaling cannot effectively correct for the many nonlinear effects in the imaging and biological system, including, for instance, the pH of the tumor microenvironment and the presence of two photo states of PpIX [2, 63], nor can it account for wavelength-dependent effects.

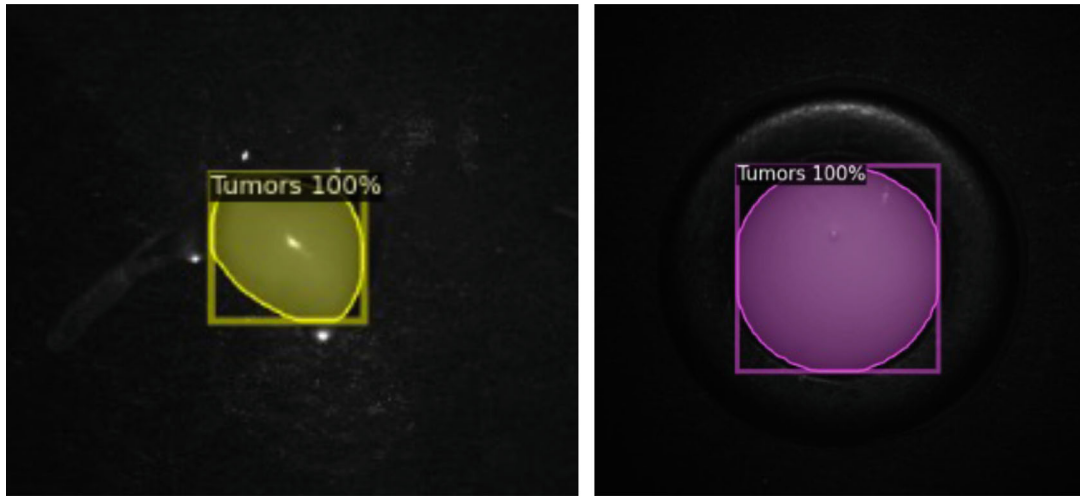


Fig. 6 Example segmentations of brain tumor biopsies on the slides using a Detectron2-based model

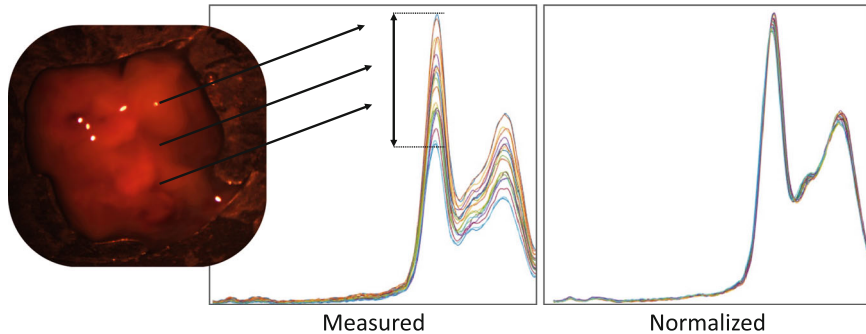


Fig. 7 Measured spectra (left) have large variance in magnitude even if taken from a nominally constant-concentration phantom. This is due to heterogeneous optical properties such as specular reflectance, shadows, and

differences in depth, as seen on the far left. After normalization, this variance is decreased (right) in phantom measurements of constant fluorophore concentration

Therefore, deep learning-based methods may be more appropriate. Only very preliminary work has been performed for this task. For this research, phantom data and pig brain homogenates with known PpIX concentrations were used, as described previously [39]. This allowed us to compare the coefficient of determination (R) of calculated PpIX abundance versus known concentration using different normalizations. The dual-band normalization and two possible learning-based normalizations that were tested are illustrated in Fig. 8. Method 2 inputs the white-light spectrum into a deep learning model to regress either a scaling factor or a scaling vector. The scaling vector has the

same dimension as the fluorescence spectrum and can be used through element-wise multiplication to perform wavelength-dependent normalization. Alternatively, in Method 3, the white-light and fluorescence spectra are stacked and input to the model, and a normalized spectrum is output directly.

For these methods, we tested MLPs and 1D CNNs. CNNs have successfully been applied to tasks such as unmixing hyperspectral images [64] into endmember abundances and directly regressing hyperspectral images to chemical concentrations [18]. In particular, CNNs are more effective at disregarding noise in spectral data compared to conventional spectral imaging chemometrics

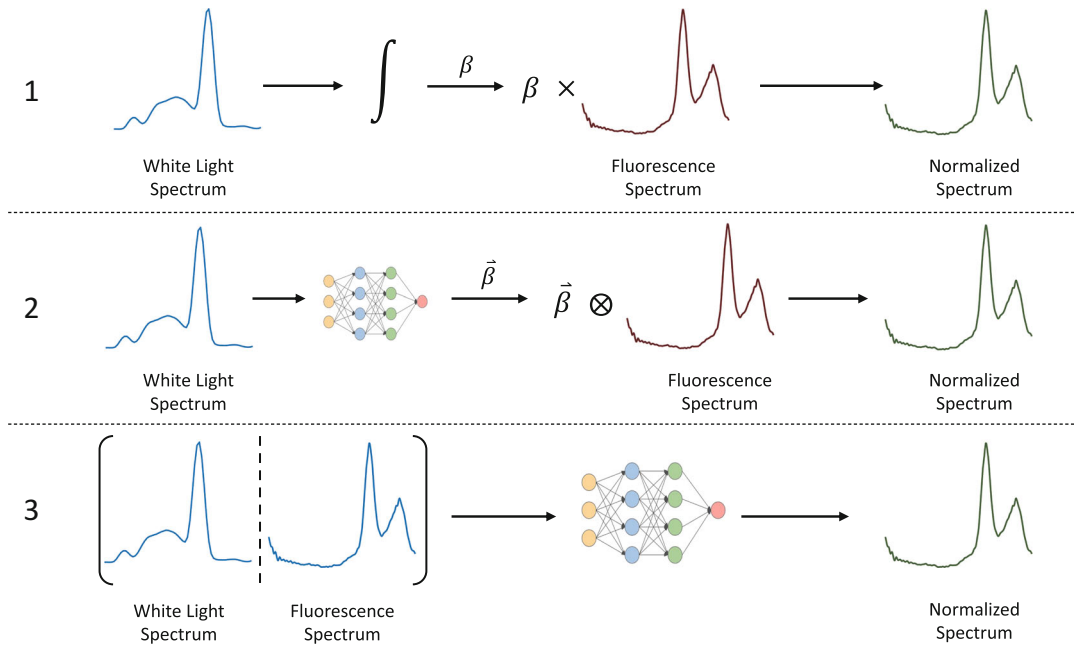


Fig. 8 We have explored three main normalization methods: (1) scaling by a factor found by integrating sections of the white-light spectrum [61], (2) scaling each wavelength independently with a vector derived from the white-light

spectrum by a deep neural network (element-wise product of $\vec{\beta}$ with the measured spectrum), and (3) outputting a scaled spectrum directly from a deep neural network whose input is the white and fluorescence spectra

techniques [18]. We also explored incorporating other architectures, such as skipping connections, which allow for bypasses of certain layers [65] or inception blocks [66] to improve model performance. These methods have been demonstrated to improve the quality and robustness of learned features [65, 66]. The best-performing model incorporated residual connections and is shown in Fig. 10.

The models were trained to minimize the mean squared error between spectra of equal known concentration and between the computed and known concentrations. It was found that outputting a scaling was difficult because, for spectra with a very small PpIX concentration, small fluctuations in the fluorescence could cause the computed PpIX abundance to be zero, leading to near-infinite scaling factors which bias the training. Excluding the low concentrations is also problematic, as it is essential to determine the precise PpIX concentration in these samples. However, when considering the pipeline of normalization followed by unmixing, it is

possible to skip this intermediate representation of a scaling factor and directly output the unmixed abundances. This is described in Sect. 7 and called the Attenuation Correction and Unmixing Network (ACU-Net) [42]. On the other hand, having an effective data-driven normalization would be very useful for applications which directly use the spectra rather than the unmixed abundances. Furthermore, the model's generalization and explainability would improve if an intermediate step were a coherent normalized spectrum. This is therefore explored in a third architecture, described in Sect. 7, known as Attenuation Correction and Unmixing by Spectrally informed Autoencoding (ACU-SA). Further development of this concept is required in future work.

7 Spectral Unmixing

As described above, the measured spectrum at a pixel is a combination of the emission spectra

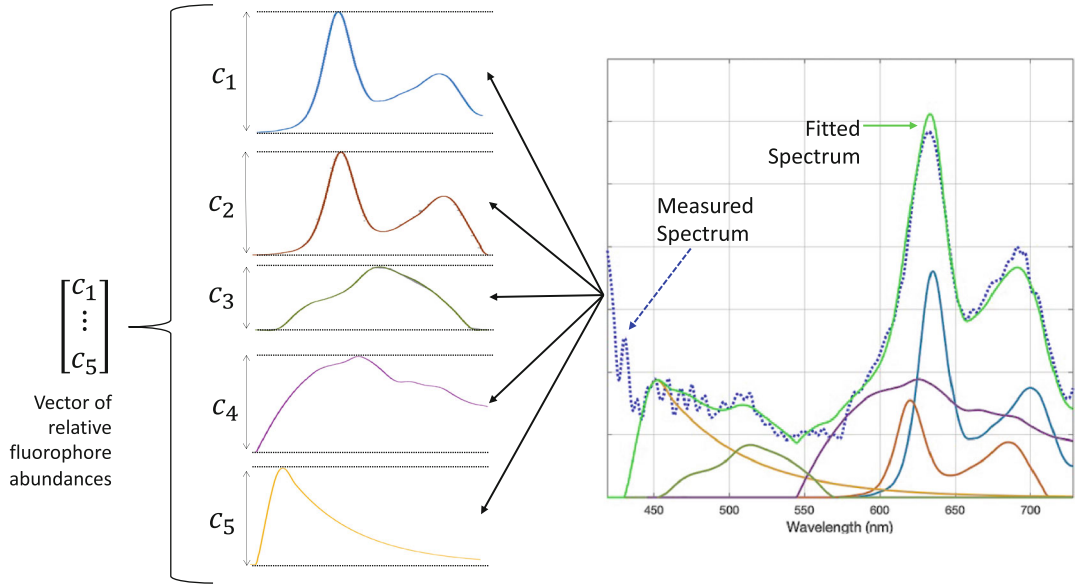


Fig. 9 Unmixing of measured spectra involves finding the linear combination of a priori known basis spectra that best fits the measured spectrum. This gives a relative

of all the fluorophores present in the pixel. Assuming the combination is linear, it is simply the weighted sum, where each spectrum's weight is the relative abundance of that fluorophore. This is illustrated in Fig. 9.

Since every measured spectrum can be expressed as a linear combination of the linearly independent fluorophore spectra, these form a basis for the space of fluorescence measurements and are called basis spectra or endmembers. With the basis spectra as the columns of a matrix B , a measurement x can be expressed as

$$x = Bc + z$$

where c is the vector of abundances, as in Fig. 9, and z is noise. To find c we can use numerical optimization methods. Many methods are possible, including robust regression to minimize the worst-case error due to noise [67] or maximum likelihood estimation [68]. In practice, fast non-negative least squares [69] is commonly used because it is simple, computationally efficient, and enforces the constraint that the abundances must not be negative. Additionally, this is the maxi-

weight, or abundance, for each constituent fluorophore. The five fluorophores were described by Black et al. [43]

mum likelihood estimate under the assumption of normally distributed noise. In fact, however, it is known that the photon emission statistics are more nearly Poisson distributed rather than Gaussian [70]. Additionally, it can be argued that a given spectrum will likely contain a few fluorophores at most, so the unmixing should reward sparsity. Therefore, low-rank Poisson regression has also been proposed for biological spectral unmixing [71]. This method led to improved accuracy on several datasets [72].

On the other hand, it is also possible to combine the normalization and unmixing using deep neural networks. Unmixing in geoscience applications has been explored using simple MLPs [73], CNNs [64, 74], and auto-associative neural networks [75], and recent work has found more success with autoencoder architectures [76]. However, the work so far is relatively preliminary and does not consider medical applications. Therefore, the architecture shown in Fig. 10 was trained on phantom and pig brain data with ground truth PpIX concentrations to perform this task. Compared to a benchmark method consisting of dual-band normalization

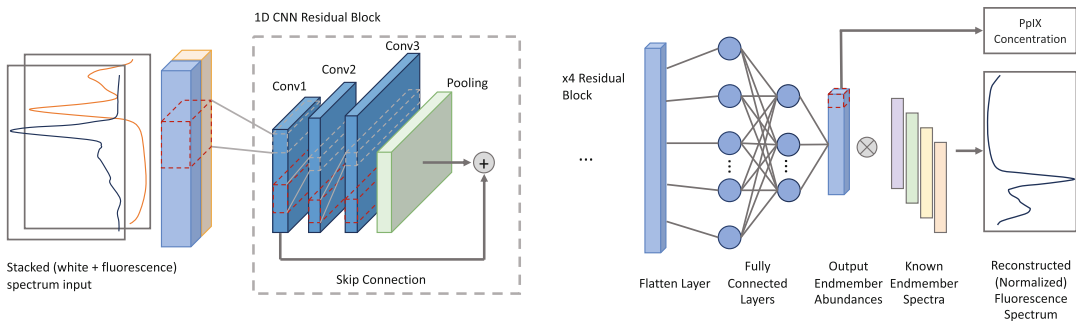


Fig. 10 Architecture for learning-based normalization and unmixing. The final output is the vector of fluorophore

abundances, and an intermediate layer can be shaped to contain the unmixed spectra. However, the latter requires further work

Table 2 Comparison of proposed end-to-end learning-based normalization and unmixing compared to the benchmark dual-band normalization followed by nonnegative least squares unmixing

	Benchmark	CNN method	Unsupervised method
Phantom data	$R^2 = 0.93$	$R^2 = \textbf{0.997}$	$R^2 = 0.98$
Pig brain homogenate	$R^2 = 0.82$	$R^2 = \textbf{0.99}$	$R^2 = 0.91$

The coefficient of determination between known and computed PpIX concentration is used for consistency with previous normalization work [62, 77]

and nonnegative least squares, this method achieved much better results. This is shown in Table 2.

While the results are very promising, extending the method to human data is nontrivial. Transfer learning approaches can be used, but the patient data lacks ground truth PpIX abundances. If the abundances computed from the classical methods are used as labels, the model will never outperform the classical method. To overcome this problem, unsupervised or semi-supervised methods can be used. One promising architecture is shown in Fig. 11 [42]. This uses an MLP to perform the normalization before passing the spectra to an encoder, which performs the unmixing. Using a weighted sum of the endmember spectra with the encoder outputs as weights can provide a reconstruction loss to train the network. The encoder can simultaneously be trained to produce independent outputs or encourage sparsity by inputting the pure endmember spectra

to an encoder with shared weights and applying a corresponding loss function to the outputs of a softmax function. In the ideal case, an input endmember spectrum will produce a vector of zeros with a one in the corresponding position. This work is still preliminary, but the results already greatly outperform the benchmark method [61] and are comparable to the fully supervised method as shown in Table 2. The method can also be pre-trained on supervised phantom or animal data using the known concentrations and encoder outputs and then extended to human data using the unsupervised reconstruction and endmember losses.

Qualitatively, the learning-based method improves results by predicting more reasonable values on human tissue data than the existing methods. An example is shown in Fig. 12. In summary, deep learning methods are promising for normalizing and unmixing measured spectra into fluorophore abundances for FGR. Much more work is possible in this direction.

8 Machine Learning Applications

With the measured spectra fully processed and unmixed, it is now possible to interpret the results. The obvious next step is plotting a PpIX concentration heatmap to show likely regions of high malignancy. However, the exact relation between PpIX abundance and tumor cell density or other

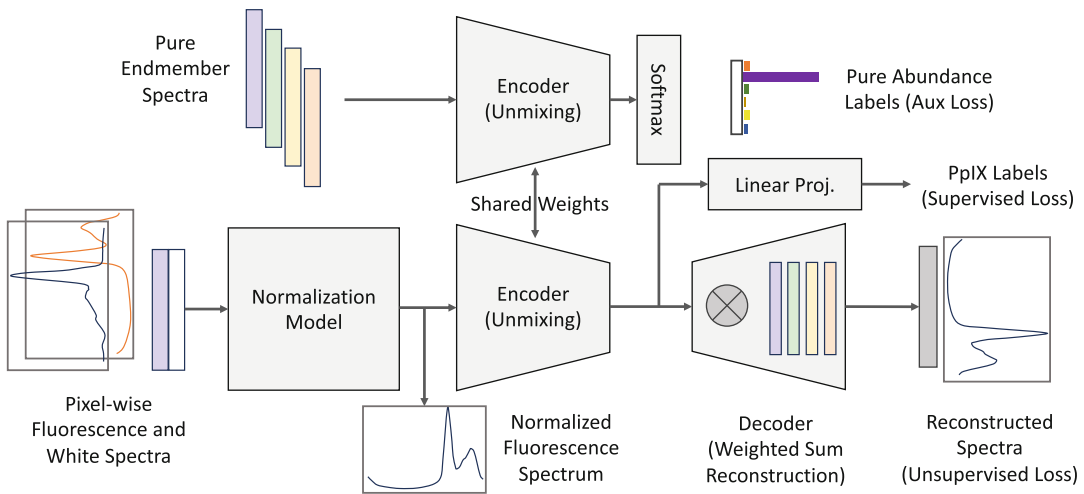


Fig. 11 Encoder-decoder model for normalization and unmixing without ground truth concentration data. The decoder can be replaced with a simple weighted sum of the endmember spectra using the encoder outputs

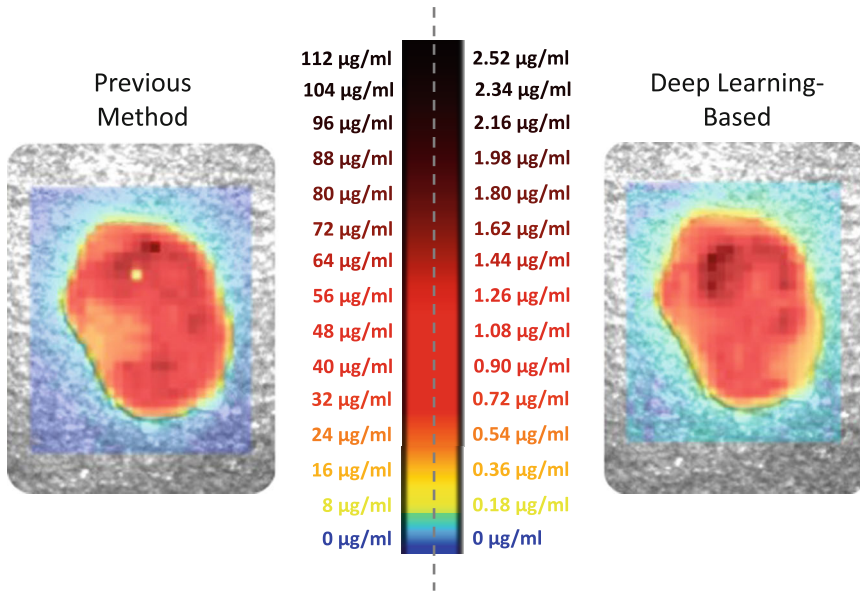


Fig. 12 From qualitative examination of several typical examples like the one shown here, deep learning-based PpIX abundance computation produces more reasonable values on human data than classical methods do when

calibrated with phantom samples of known absolute concentration. The normalization is also better, as the brightly reflecting point in the top center is smoothed out

clinically relevant measures is unknown. Furthermore, it is possible to obtain much more fine-grained information from the fluorophore abundances. This is one of the most exciting applications for machine learning in HSI for FGR. The following outlines some of the main findings

from Black et al. [41], which built upon Leclerc et al. [40].

Even with the previously described five fluorophore abundances [43], it is still impossible to visualize the unmixing result; further dimensionality reduction is required. Figure 13 shows

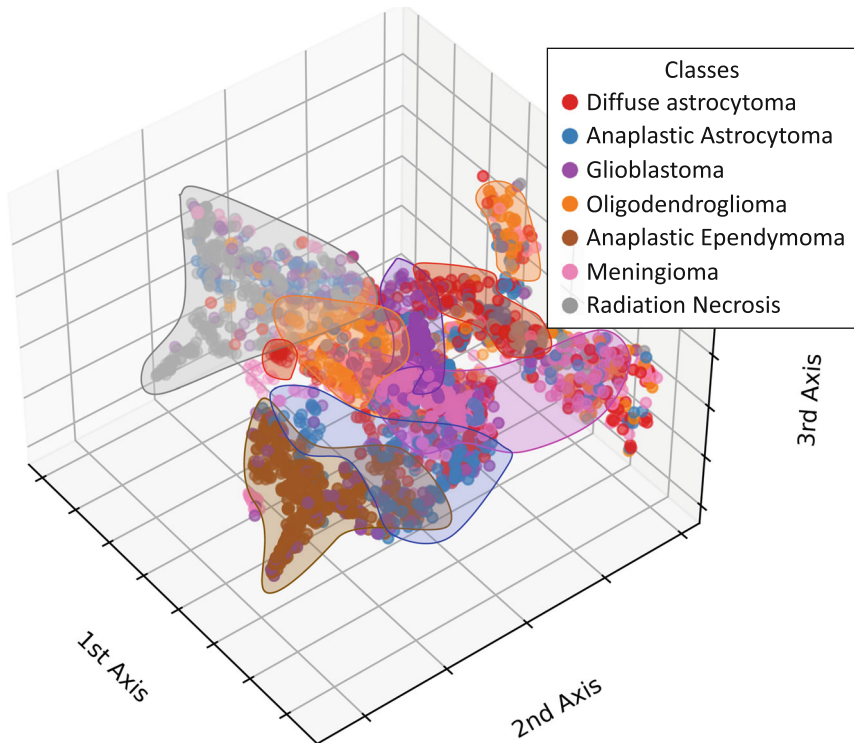


Fig. 13 t-SNE plot of the spectra of different tumor types, showing some relatively clear clusterings

the result of t-SNE reduction to only three dimensions, in which some clusters are nonetheless clearly visible. This is promising for tumor type classification. In addition, it was found that the first five components of PCA contain 97–99% of the variance of the original spectra, showing that five values can indeed effectively describe the information content of a whole fluorescence spectrum. With the five fluorophore abundances, four machine learning models were trained and tested on the data outlined in Table 1. The four tasks were classification of tumor type, margin type, WHO grade, and IDH mutation. The dataset was split 80/20 for training and testing, and five-fold cross-validation was used for hyperparameter tuning and model selection. MLP, random forest, KNN, and SVM models were tested for each task. All the values reported below are results on the test set.

A random forest classifier with 150 trees performed best on the tumor type tests, with 87.3% accuracy and an average area under curve (AUC)

of the receiver operating characteristic (ROC) curve of 0.98. We experimented with grouping at a higher level by combining the various astrocytoma, glioma, and glioblastoma data cubes under the broad label of glioma. An MLP with three hidden layers could classify between glioma, meningioma, medulloblastoma, and radiation necrosis with 90% accuracy and an AUC of 0.97. The confusion charts of these two classifications are shown in Fig. 14.

For margin classification, an MLP network was able to classify solid tumor, infiltrating zone, and reactively altered brain tissue (RABT) with 85.7% accuracy and an AUC of 0.95. Though still excellent, the slightly lower accuracy is likely due to the continuous nature of these classes, making rigid distinctions difficult, even for pathologists. In this test, RABT is effectively the healthy tissue class because normal healthy brain tissue is not removed during surgery and thus cannot be imaged on the ex vivo HSI device, and RABT is noncancerous.

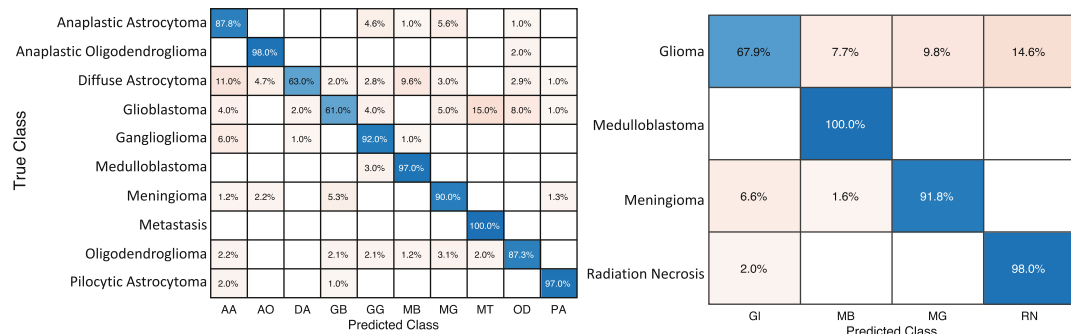


Fig. 14 Confusion matrices of two different tumor type classifiers, once with all available tumor classes in the dataset and once with broader categories, both showing good performance

An MLP also achieved 96.1% accuracy in determining the WHO grade of the tumor biopsies, with an AUC of 0.99. Finally, a random forest model classified IDH mutant and wildtype tumors with 93% accuracy and an AUC of 0.98.

These results show great promise for intraoperative classification systems, not only for whether a region of tissue is healthy or malignant but also for informing the surgeon of the type of tissue or tumor, the grade of the cancer, and whether it is IDH wildtype or mutant. This information can guide the resection not only in terms of location but also in terms of the extent of the resection. Tumors with different WHO grades or IDH mutation status can have very different prognoses and might thus warrant more or less aggressive resection. Other biomarkers may also be classified accurately from HSI data. Bringing all of this information to the surgeon intraoperatively can significantly improve the resection of brain tumors (Fig. 15).

9 Conclusion and Future Outlook

Much progress remains to be made in all of the applications of machine learning and data-driven computational methods for HSI in fluorescence-guided brain tumor resection described in this chapter. The described methods for normalization and unmixing constitute preliminary research, and more work is needed

in applying modern deep learning techniques to HSI FGR. In particular, the medical HSI literature outlined in the introduction focuses on semantic segmentation of *in vivo* images, but this has not yet been done in FGR. In fact, none of the methods described in this chapter used the spatial information in the data cubes other than to draw overlay plots. To do this, however, larger and more diverse datasets are required. The dataset presented in this chapter is relatively large in this field but still small compared to other medical imaging and general computer vision datasets. It also stems from a single device at a single center. One aspect that will greatly facilitate the creation of larger datasets by decreasing the acquisition time of the data cubes is the further development of high-resolution snapshot HSI cameras, both from a hardware and software standpoint, as described in Sect. 4.

This advancement will also enable the integration of HSI systems intraoperatively. Indeed, much of the work so far on this topic has been on *ex vivo* data or very limited, disruptive *in vivo* imaging of a few patients. Future work must focus on clinical translation and practical use. This also includes identifying outputs from such a system that are practically relevant to the operation. For example, intraoperative knowledge of the IDH mutation might change the surgeon's approach. Furthermore, while imaging systems are being developed to recognize tumor margins, the extent of tumor margins is, due to the infiltrative nature of these tumors, not in themselves well defined,

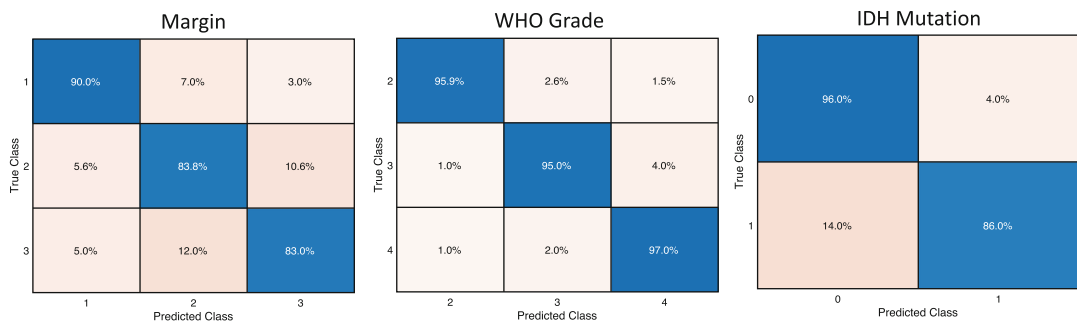


Fig. 15 Confusion matrices of margin, WHO grade, and IDH mutation classifiers. The margin labels are 1 (solid tumor), 2 (infiltrating zone), and 3 (reactively altered brain

tumor) (effectively, healthy tissue). WHO grades II, III, and IV were included (insufficient data on grade I tumors was available), and an IDH value of 0 indicates a wildtype, while 1 indicates an IDH mutation

as the cancer transitions relatively continuously from solid tumor to infiltrating zone with decreasing tumor cell density. No binary threshold exists between “tumor” and “not tumor.” Thus, perhaps a mapping from fluorophore abundances to tumor cell density would be more appropriate. This could be shown to the surgeon to give them the full picture while leaving the extent of resection up to their discretion. This has not yet been done due to the difficulty of counting tumor cell density in pathological slides and then spatially registering these with the hyperspectral images. Still, it should be the target of future efforts. For this question, a better understanding of the two photo states of PpIX could also be valuable [2], and data-driven methods will surely be essential.

Ultimately, hyperspectral fluorescence imaging holds great promise for improving the outcomes of brain tumor surgery. In combination with machine learning and data-driven computational approaches, many improvements are possible, not only to the processing of the data but also to the image acquisition itself and, importantly, to the interpretation and analysis of the rich output data. This can be used to determine the tissue type, its level of malignancy, WHO grade, IDH mutation, and myriad other important biomarkers. With some further development, these technologies can potentially benefit patient care substantially.

Acknowledgments We would like to thank Carl Zeiss Meditec (Oberkochen, Germany) for providing us with

the required BLUE400 filter and the OPMI PICO system, as well as Sadahiro Kaneko and Anna Walke for the assistance in the data collection.

References

1. Stepp H, Stummer W. 5-ALA in the management of malignant glioma. *Lasers Surg Med*. 2018;50(5):399–419. <https://doi.org/10.1002/lsm.22933>.
2. Suero Molina E, Black D, Walke A, et al. Unraveling the blue shift in porphyrin fluorescence in glioma: the 620 nm peak and its potential significance in tumor biology. *Front Neurosci*. 2023;17:1261679. <https://doi.org/10.3389/fnins.2023.1261679>.
3. Stummer W, Pichlmeier U, Meinel T, et al. Fluorescence-guided surgery with 5-aminolevulinic acid for resection of malignant glioma: a randomised controlled multicentre phase III trial. *Lancet Oncol*. 2006;7(5):392–401. [https://doi.org/10.1016/S1470-2045\(06\)70665-9](https://doi.org/10.1016/S1470-2045(06)70665-9).
4. Schupper AJ, Rao M, Mohammadi N, et al. Fluorescence-guided surgery: a review on timing and use in brain tumor surgery. *Front Neurol*. 2021;12:682151. <https://doi.org/10.3389/fneur.2021.682151>.
5. Qian S-E. Hyperspectral satellites, evolution, and development history. *IEEE J Sel Topics Appl Earth Obsr Rem Sens*. 2021;14:7032–56.
6. Lu B, Dao PD, Liu J, He Y, Shang J. Recent advances of hyperspectral imaging technology and applications in agriculture. *Rem Sens*. 2020;12(16):2659.
7. Adão T, Hruška J, Pádua L, et al. Hyperspectral imaging: a review on UAV-based sensors, data processing and applications for agriculture and forestry. *Remote Sens*. 2017;9(11):1110.
8. ElMasry G, Sun D-W. Principles of hyperspectral imaging technology. *Hyperspect Imaging Food Qual Anal Contr*. Elsevier. 2010:3–43.

9. Aggarwal SLP, Papay FA. Applications of multispectral and hyperspectral imaging in dermatology. *Exp Dermatol.* 2022;31(8):1128–35.
10. Leiloglou M, Kedrzycki M, Chalau V, Shanthakumar D, Elson D, Leff D. 5-ALA induced fluorescence imaging for margin status identification during breast conserving surgery. *Eur J Surg Oncol.* 2023;49:e220. <https://doi.org/10.1016/j.ejso.2023.03.019>.
11. Clancy NT, Jones G, Maier-Hein L, Elson DS, Stoyanov D. Surgical spectral imaging. *Med Image Anal.* 2020;63:101699. <https://doi.org/10.1016/J.MEDIA.2020.101699>.
12. Li J, Bioucas-Dias JM, Plaza A. Hyperspectral image segmentation using a new Bayesian approach with active learning. *IEEE Trans Geosci Rem Sens.* 2011;49(10):3947–60.
13. Nalepa J, Myller M, Kawulok M. Validating hyperspectral image segmentation. *IEEE Geosci Rem Sens Lett.* 2019;16(8):1264–8.
14. Sun H, Zheng X, Lu X. A supervised segmentation network for hyperspectral image classification. *IEEE Trans Image Process.* 2021;30:2810–25.
15. Tarabalka Y, Chanussot J, Benediktsson JA. Segmentation and classification of hyperspectral images using watershed transformation. *Pattern Recog.* 2010;43(7):2367–79.
16. Calin MA, Boiangiu IC, Parasca SV, Miclos S, Savastru D, Manea D. Blood oxygenation monitoring using hyperspectral imaging after flap surgery. *Spectrosc Lett.* 2017;50(3):150–5.
17. Goodfellow I, Bengio Y, Courville A. Deep learning. MIT Press; 2016.
18. Jia S, Jiang SG, Lin ZJ, Li NY, Xu M, Yu SQ. A survey: deep learning for hyperspectral image classification with few labeled samples. *Neurocomputing.* 2021;448:179–204. <https://doi.org/10.1016/j.neucom.2021.03.035>.
19. Cui R, Yu H, Xu T, et al. Deep learning in medical hyperspectral images: a review. *Sensors.* 2022;22:9790. <https://doi.org/10.3390/S22249790>.
20. Khan U, Paheding S, Elkin CP, Devabhaktuni VK. Trends in deep learning for medical hyperspectral image analysis. *IEEE Access.* 2021;9:79534–48. <https://doi.org/10.1109/ACCESS.2021.3068392>.
21. Ebner M, Nabavi E, Shapey J, et al. Intraoperative hyperspectral label-free imaging: from system design to first-in-patient translation. *J Phys D: Appl Phys.* 2021;54:294003. <https://doi.org/10.1088/1361-6463/ABFBF6>.
22. Ruiz L, Martin A, Urbanos G, et al. Multi-class brain tumor classification using hyperspectral imaging and supervised machine learning. 2020 35th conference on design of circuits and integrated systems, DCIS 2020. <https://doi.org/10.1109/DCIS51330.2020.9268650>.
23. Urbanos G, Martín A, Vázquez G, et al. Supervised machine learning methods and hyperspectral imaging techniques jointly applied for brain cancer classification. *Sensors.* 2021;21:3827. <https://doi.org/10.3390/S21113827>.
24. Fabelo H, Halicek M, Ortega S, et al. Deep learning-based framework for in vivo identification of glioblastoma tumor using hyperspectral images of human brain. *Sensors.* 2019;19:920. <https://doi.org/10.3390/S19040920>.
25. Fabelo H, Ortega S, Ravi D, et al. Spatio-spectral classification of hyperspectral images for brain cancer detection during surgical operations. *PLOS One.* 2018;13:e0193721. <https://doi.org/10.1371/JOURNAL.PONE.0193721>.
26. Leon R, Fabelo H, Ortega S, et al. Hyperspectral imaging benchmark based on machine learning for intraoperative brain tumour detection. *npj Precision Oncol.* 2023;7:1–17. <https://doi.org/10.1038/s41698-023-00475-9>.
27. Rinesh S, Maheswari K, Arthi B, et al. Investigations on brain tumor classification using hybrid machine learning algorithms. *J Healthcare Eng.* 2022;2761847. <https://doi.org/10.1155/2022/2761847>.
28. Fabelo H, Ortega S, Szolna A, et al. In-vivo hyperspectral human brain image database for brain cancer detection. *IEEE Access.* 2019;7:39098–116.
29. Manni F, van der Sommen F, Fabelo H, et al. Hyperspectral imaging for glioblastoma surgery: improving tumor identification using a deep spectral-spatial approach. *Sensors.* 2020;20:6955. <https://doi.org/10.3390/S20236955>.
30. Hao Q, Pei Y, Zhou R, et al. Fusing multiple deep models for in vivo human brain hyperspectral image classification to identify glioblastoma tumor. *IEEE Trans Instrum Measure.* 2021;70. <https://doi.org/10.1109/TIM.2021.3117634>.
31. Callicó GM, Camacho R, MdIL P, Ortega S, Sarmiento R, Fabelo H. Detecting brain tumor in pathological slides using hyperspectral imaging. *Biomed Optics Exp.* 2018;9(2):818–31. <https://doi.org/10.1364/BOE.9.000818>.
32. Puustinen S, Vrzáková H, Hyttinen J, et al. Hyperspectral imaging in brain tumor surgery—evidence of machine learning-based performance. *World Neurosurg.* 2023;175:e614–35. <https://doi.org/10.1016/J.WNEU.2023.03.149>.
33. Kifle N, Teti S, Ning B, et al. Pediatric brain tissue segmentation using a snapshot hyperspectral imaging (sHSI) camera and machine learning classifier. *Bioengineering.* 2023;10:1190. <https://doi.org/10.3390/BIOENGINEERING10101190>.
34. Ronneberger O, Fischer P, Brox T. U-net: convolutional networks for biomedical image segmentation. Springer; 2015. p. 234–41.
35. Milletari F, Navab N, Ahmadi S-A. V-net: fully convolutional neural networks for volumetric medical image segmentation. *IEEE.* 2016:565–71.
36. Li Y, Zhang Y, Cui W, Lei B, Kuang X, Zhang T. Dual encoder-based dynamic-channel graph convolutional network with edge enhancement for retinal vessel segmentation. *IEEE Trans Med Imaging.* 2022;41(8):1975–89.

37. Xun S, Li D, Zhu H, et al. Generative adversarial networks in medical image segmentation: a review. *Comp Biol Med.* 2022;140:105063.
38. Zhou Q, Wang Q, Bao Y, Kong L, Jin X, Ou W. Laednet: a lightweight attention encoder–decoder network for ultrasound medical image segmentation. *Comp Electr Eng.* 2022;99:107777.
39. Walke A, Black D, Valdes PA, Stummer W, Konig S, Suero-Molina E. Challenges in, and recommendations for, hyperspectral imaging in ex vivo malignant glioma biopsy measurements. *Sci Rep.* 2023;13(1):3829. <https://doi.org/10.1038/s41598-023-30680-2>.
40. Leclerc P, Ray C, Mahieu-Willame L, et al. Machine learning-based prediction of glioma margin from 5-ALA induced PpIX fluorescence spectroscopy. *Sci Rep.* 2020;10(1):1462. <https://doi.org/10.1038/s41598-020-58299-7>.
41. Black D, Byrne D, Walke A, et al. Towards machine learning-based quantitative hyperspectral image guidance for brain tumor resection. 2023.
42. Black D, Gill J, Xie A, et al. Deep learning-based correction and unmixing of hyperspectral images for brain tumor surgery. 2024:arXiv:2402.03761. <https://doi.org/10.48550/arXiv.2402.03761>. <https://ui.adsabs.harvard.edu/abs/2024arXiv240203761B>. Accessed 1 Feb 2024.
43. Black D, Kaneko S, Walke A, Konig S, Stummer W, Suero ME. Characterization of autofluorescence and quantitative protoporphyrin IX biomarkers for optical spectroscopy-guided glioma surgery. *Sci Rep.* 2021;11(1):20009. <https://doi.org/10.1038/s41598-021-99228-6>.
44. Amigo JM, Babamoradi H, Elcoroaristizabal S. Hyperspectral image analysis. A tutorial. *Analytica Chimica Acta.* 2015;896:34–51.
45. Wang L, Zhao C. Hyperspectral image processing. Springer; 2016.
46. Kaneko S, Molina ES, Sporns P, Schipmann S, Black D, Stummer W. Fluorescence real-time kinetics of protoporphyrin IX after 5-ALA administration in low-grade glioma. *J Neurosurg.* 2021;1(aop):1–7.
47. Molina ES, Black D, Kaneko S, Müther M, Stummer W. Double dose of 5-aminolevulinic acid and its effect on protoporphyrin IX accumulation in low-grade glioma. *J Neurosurg.* 2022;137(4):943–52.
48. Molina ES, Kaneko S, Black D, Stummer W. 5-Aminolevulinic acid-induced porphyrin contents in various brain tumors: implications regarding imaging device design and their validation. *Neurosurgery.* 2021;89(6):1132–40.
49. Qin J. Hyperspectral imaging instruments. *Hyperspectral Imaging Food Qual Anal Contr.* Elsevier. 2010;129–72.
50. Lim H-T, Murukeshan VM. Spatial-scanning hyperspectral imaging probe for bio-imaging applications. *Rev Sci Instrum.* 2016;87(3).
51. Kester RT, Bedard N, Gao L, Tkaczyk TS. Real-time snapshot hyperspectral imaging endoscope. *J Biomed Optics.* 2011;16(5):056005-056005-12.
52. Bodkin A, Sheinis A, Norton A, Daly J, Beaven S, Weinheimer J. Snapshot hyperspectral imaging: the hyperpixel array camera. *SPIE.* 2009;164–74.
53. Jeon DS, Baek S-H, Yi S, et al. Compact snapshot hyperspectral imaging with diffracted rotation. 2019.
54. Martinez B, Leon R, Fabelo H, et al. Most relevant spectral bands identification for brain cancer detection using hyperspectral imaging. *Sensors.* 2019;9:5481. <https://doi.org/10.3390/S19245481>.
55. Baig N, Fabelo H, Ortega S, Callico GM, Alirezai J, Umapathy K. Empirical mode decomposition based hyperspectral data analysis for brain tumor classification. *Proc Annual Int Conf IEEE Eng Med Biol Soc EMBS.* 2021;2274–7. <https://doi.org/10.1109/EMBC46164.2021.9629676>.
56. Giannantonio T, Alperovich A, Semeraro P, et al. Intra-operative brain tumor detection with deep learning-optimized hyperspectral imaging. 2023;12373:80–98. <https://doi.org/10.1117/12.2646999>.
57. Li P, Ebner M, Noonan P, et al. Deep learning approach for hyperspectral image demosaicking, spectral correction and high-resolution RGB reconstruction. *Comp Meth Biomech Biomed Eng: Imag Visual.* 2022;10:409–17. <https://doi.org/10.1080/21681163.2021.1997646>.
58. Li P, Asad M, Horgan C, MacCormac O, Shapey J, Vercauteren T. Spatial gradient consistency for unsupervised learning of hyperspectral demosaicking: application to surgical imaging. *Int J Comp Assist Radiol Surg.* 2023;18:981–8. <https://doi.org/10.1007/S11548-023-02865-7/TABLES/2>.
59. Budd C, Qiu J, MacCormac O, et al. Deep reinforcement learning based system for intraoperative hyperspectral video autofocusing. *Lecture notes in computer science (including subseries Lecture notes in artificial intelligence and Lecture notes in bioinformatics).* 2023;14228 LNCS:658–67. https://doi.org/10.1007/978-3-031-43996-4_63/TABLES/1
60. Detectron2. 2019. <https://github.com/facebookresearch/detectron2>
61. Valdés PA, Leblond F, Kim A, Wilson BC, Paulsen KD, Roberts DW. A spectrally constrained dual-band normalization technique for protoporphyrin IX quantification in fluorescence-guided surgery. *Opt Lett.* 2012;37(11):1817–9. <https://doi.org/10.1364/OL.37.001817>.
62. Valdés PA, Leblond F, Jacobs VL, Wilson BC, Paulsen KD, Roberts DW. Quantitative, spectrally-resolved intraoperative fluorescence imaging. *Sci Rep.* 2012;2(1):798.
63. Alston L, Mahieu-Willame L, Hebert M, et al. Spectral complexity of 5-ALA induced PpIX fluorescence in guided surgery: a clinical study towards the discrimination of healthy tissue and margin boundaries in high and low grade gliomas. *Biomed Optics Exp.* 2019;10(5):2478–92.
64. Zhang X, Lin T, Xu J, Luo X, Ying Y. DeepSpectra: an end-to-end deep learning approach for quantitative

- spectral analysis. *Anal Chim Acta*. 2019;1058:48–57. <https://doi.org/10.1016/j.aca.2019.01.002>.
- 65. He KM, Zhang XY, Ren SQ, Sun J. Deep residual learning for image recognition. *Proc CVPR IEEE*. 2016;:770–8. <https://doi.org/10.1109/Cvpr.2016.90>.
 - 66. Szegedy C, Vanhoucke V, Ioffe S, Shlens J, Wojna Z. Rethinking the inception architecture for computer vision. *Proc CVPR IEEE*. 2016;:2818–26. <https://doi.org/10.1109/Cvpr.2016.308>.
 - 67. Li G. Robust regression. Exploring data tables, trends, and shapes. 1985;281:U340.
 - 68. Myung IJ. Tutorial on maximum likelihood estimation. *J Math Psychol*. 2003;47(1):90–100.
 - 69. Geladi P, Kowalski BR. Partial least-squares regression – a tutorial. *Analytica Chimica Acta*. 1986;185:1–17. [https://doi.org/10.1016/0003-2670\(86\)80028-9](https://doi.org/10.1016/0003-2670(86)80028-9).
 - 70. Coates P. Photomultiplier noise statistics. *J Phys D: Appl Phys*. 1972;5(5):915.
 - 71. Wang R, Lemus AA, Henneberry CM, Ying Y, Feng Y, Valm AM. Unmixing biological fluorescence image data with sparse and low-rank Poisson regression. *Bioinformatics*. 2023;39(4):btad159.
 - 72. Black D, Liquet B, Kaneko S, Di Leva A, Stummer W, Suero Molina E. A spectral library and method for sparse unmixing of hyperspectral images in fluorescence guided resection of brain tumors. 2024:arXiv:2401.17388. <https://doi.org/10.48550/arXiv.2401.17388>. <https://ui.adsabs.harvard.edu/abs/2024arXiv240117388B>. Accessed 1 Jan 2024.
 - 73. Vijayashekhar SS, Deshpande VS, Bhatt JS. A practical approach for hyperspectral unmixing using deep learning. *IEEE Geosci Rem Sens Lett*. 2022;19:ArtN 5511505. <https://doi.org/10.1109/Lgrs.2021.3127075>.
 - 74. Zhang XR, Sun YJ, Zhang JY, Wu P, Jiao LC. Hyperspectral unmixing via deep convolutional neural networks. *IEEE Geosci Rem Sens Lett*. 2018;15(11):1755–9. <https://doi.org/10.1109/Lgrs.2018.2857804>.
 - 75. Licciardi GA, Del Frate F. Pixel unmixing in hyperspectral data by means of neural networks. *IEEE Trans Geosci Rem Sens*. 2011;49(11):4163–72. <https://doi.org/10.1109/Tgrs.2011.2160950>.
 - 76. Hong D, Gao L, Yao J, et al. Endmember-guided unmixing network (EGU-Net): a general deep learning framework for self-supervised hyperspectral unmixing. *IEEE Trans Neural Netw Learn Syst*. 2022;33(11):6518–31. <https://doi.org/10.1109/TNNLS.2021.3082289>.
 - 77. Valdés P, Leblond F, Kim A, Wilson B, Paulsen K, Roberts D. A spectrally constrained dual-band normalization technique for protoporphyrin IX quantification in fluorescence-guided surgery. *Optics Lett*. 2012;37(11):1817–9.